Design of constant temperature cooling device for melanoma screening by dynamic thermography

T. Gomboc [1], J. Iljaž [*1], L. C. Wrobel [2], M. Hriberšek [1] and J. Marn [1]

1 – Faculty of Mechanical Engineering, University of Maribor

Smetanova 17, SI-2000 Maribor, Slovenia, * corresp: jurij.iljaz@um.si

2 – Department of Civil and Environmental Engineering,

PUC-Rio - Pontifical Catholic University of Rio de Janeiro,

Rua Marquês de São Vicente 225, Rio de Janeiro, Brazil

January 13, 2021

Abstract

Dynamic thermography is a promising new non-invasive diagnostic technique for melanoma screening. This paper proposes a novel experimental setup of an active cooling device for dynamic thermography using a metal disc and a Peltier module. The aim is to achieve constant cooling temperature that induce deep cooling penetration and, therefore, better thermal contrast. The paper covers the numerical analysis of the device design parameters like thermocouple position, disc thickness and regulation coefficient prior to building it. Simulation is based on a numerical model of skin tissue with melanoma and the metal disc. The Peltier module has been modeled indirectly through a boundary condition simulating the device active cooling. For effective solving of the direct problem, the BEM has been used. Results showed that the thermocouple position for cooling regulation is not as important as the value of the regulation coefficient or disc thickness. A thicker disc improves the initial cooling due to higher thermal capacity. However, a thinner disc is recommended due to the faster regulation and more constant cooling temperature. Results also showed that lesion size did not affect the cooling temperature, meaning that it can be used for investigation in any tumour stage.

Keywords: Thermoelectric cooling, Constant temperature, Bio-heat, Peltier module, Dynamic thermography, Numerical design.

1 Introduction

Malignant melanoma is the most fatal type of skin cancer because it metastases rapidly and can spread to soft tissues like lung and liver [1–6]. Clark [1] classified malignant melanomas

into five levels from I to V, depending on the melanoma intrusion into certain skin layers. Clark I level represents melanoma *in situ* meaning that the cells are only in the epidermis, while Clark V has already grown into the fat layer under the skin. Survival rate of patients with melanoma is directly correlated with the level or its thickness [1,4,5,7]. The deeper the invasion, the lower the survival rate. For this reason, it is important to detect skin cancer or malignant melanoma in its early stage.

Currently, the most frequently used technique to detect melanoma is the ABCDE (Asymmetry, Border, Colour, Diameter, Evolution) method, which consists in the visual inspection of a lesion by dermatologists. The ABCDE method uses only qualitative guidelines for melanoma identification and requires a trained specialist to actually distinguish malignant melanoma from benign nevi. Therefore, this technique produces a high rate of false positive or false negative identification [5,6,8,9]. To avoid the risk of missing an early stage melanoma, excisional biopsies are routinely performed. Current statistics show that one melanoma is found in $20 - 60$ biopsies using the ABCDE method [6, 9]. To reduce the number of unnecessary biopsies, as well as to improve an early detection of melanoma, new non-invasive techniques are being researched. Some of these techniques are dermoscopy [4, 10–14], total body photography (TBP) [4, 10, 14], reflectance confocal microscopy (RCM) [4, 10, 12, 14, 15], multiphoton tomography [4], laser spectroscopy [4], dynamic thermography (DT) [4, 6, 9], multispectral imaging (MSI) [14, 16, 17], optical coherence tomography (OCT) [12, 14], electrical impedance spectroscopy (EIS) [4, 12], high frequency ultrasonography [12, 14], laser Doppler imaging (LDI) [18] and magnetic resonance imaging (MRI) [14].

In recent years thermography or infrared thermal (IRT) imaging in medicine became a very valuable tool not just for skin cancer screening and diagnostic [3, 6, 9, 19–23] but also for various different applications like breast cancer diagnostics [24–29], diagnosis of vascular disorder [26, 30] and burns diagnostic [31, 32]. Thermography in medicine is based on the temperature contrast taken with the IR camera for which a trained person is needed to interpret the thermal image correctly. This temperature contrast of IRT image is the outcome of the bioheat transfer in the observed tissue. Bioheat transfer in tissue depends on blood perfusion, metabolic heat generation, material properties and heat transfer with its surroundings. Deviation in blood perfusion rate, cell metabolism or material properties shows the physiological and pathological change and is reflected in different temperature or temperature contrast that can be detected using IR camera. Thermography can be done in two ways, passively or actively. Passive or static thermography measures the temperature of the tissue under a steady-state condition when the patient is acclimatised to the room conditions. On the other hand, active or dynamic thermography induces thermal stimulation by heating or cooling the tissue and then measuring the thermal response during the recovery phase [3, 21, 26, 28, 29, 33–36].

Dynamic thermography imaging (DTI) is showing to be a very promising non-invasive technique for skin cancer detection with specificity $> 80\%$ and 95% sensitivity [3, 6, 9]. Computer aided DTI can also help in determination of lesion parameters like size, thickness or blood perfusion [3,37–39]. Using thermal stimulation in DTI, usually cooling, increases the temperature difference or contrast between the lesion and healthy tissue during the recovery phase, which is easier to detect compared to static thermography. One of the advantages of DTI is also a quicker examination time $(2 - 3min)$ because there is no need for patient acclimatisation. Many authors showed that detection of melanoma can be done in its early stage, as well as we can screen a larger surface area or multiple lesions at the same time [3, 6, 9, 23]. Cooling is usually made by blowing cold air or applying a cooling patch at $15 - 25°C$

for up to $1min$ [9]. Çetingül and Herman [3] used DTI with a cooled gel pack at first, that has then been replaced with cold air cooling using an Exair vortex tube, which provides a stream of cold air and was more comfortable for the patient, with a cooling time of $1min$. Similarly, Godoy et al. [6] used the cold air cooling approach using a Ranque-Hilsch vortex tube for $30s$ to make a study of DTI on 102 patients. There are also other cooling approaches to cool down the skin or part of the body such as spraying of water or coolant, water immersion, ice or chilled gels, cotton patches, metal disc, etc. [21, 40–42]. In all these approaches, it is hard to control the cooling temperature or the heat flux because they are passive. Cheng and Herman [21] used a 2D numerical model to investigate the effect of different types of cooling processes. They compared numerically a constant temperature cooling approach with a cotton patch soaked in water and convective cooling using different cooling times and temperatures, observing the penetration depth. Constant cooling temperature approach reaches deepest cooling penetration among the compared approaches and produces the highest thermal contrast between the lesion and healthy skin. Therefore, it could be of great interest for the cooling process, however hard to meet in practice. The most convenient cooling approach from a practical point of view is cooling with convection (cold air stream) or evaporation (coolant spraying or soaked cotton patch), but harder to know the exact cooling parameters like heat transfer coefficient, cooling temperature on the surface, etc. These parameters are needed for computer aided DTI to simulate the cooling-rewarming process as accurately as possible. A constant temperature cooling approach is therefore appealing not only because of easier implementation for numerical analysis but also because of the higher thermal contrast during the rewarming process of DTI.

The paper investigates the possibility of a constant temperature cooling approach using a Peltier module for melanoma screening by DTI. A similar device has been developed by Strąkowska et al. [36], who used it to evaluate blood perfusion rate and thermal properties of the skin using DTI. The cooling temperature was set to $26°C$ and cooling time to $4s$, meaning low cooling penetration depth. In this paper, we numerically assess the design of a cooling device for lower cooling temperatures ($13°C$) and longer cooling times ($60s$). We analyse the effect of thermocouple position for device regulation, plate thickness, melanoma stage, and regulation degree on the achieved cooling temperature. The aim is to achieve constant cooling temperature during the cooling stage. Longer cooling process is reflected in deeper penetration depth leading to higher temperature contrast and better sensitivity of the DTI technique. The study is made on a numerical model of skin tissue already described in our previous work, including thermoregulation to obtain a more realistic tissue response [43], and solved using subdomain BEM. Simulation is done just for the cooling process, which is the focus of this research, not simulating the rewarming process. A numerical study of the cooling stage prior to the experimental setup is needed to evaluate the most important parameters of the cooling approach and device design.

The paper is organized as follows: Section 2 presents the numerical model used to evaluate the cooling device design, described by the computational domain, governing equations and boundary conditions. The subdomain BEM developed to solve the direct heat transfer problem for a 3D computational domain is described briefly in Section 3. Section 4 presents the numerical results and discusses how plate thickness, thermocouple position for regulation, tumour stage and regulation degree affect the achieved cooling temperature at the skin surface. The paper closes with Section 5, that summarizes this work and emphasizes the importance of its results.

2 Numerical model

The design of a constant temperature cooling device can be tested in two ways, experimentally or numerically. The latter approach has the advantage to test the design before the actual production, and can reveal the pros and cons of the design. For this reason, the numerical study of a cooling device presented in this paper investigates the effect of the thermocouple position, disc thickness, regulation of Peltier module and melanoma stage on the achieved cooling temperature during the DTI cooling process. Numerically tested theoretical design depends on the numerical model, which should be as realistic as possible. Therefore, the numerical model is based on the skin tissue including melanoma lesion and local thermoregulation response [43] together with the metal disc and cooling effect of Peltier module. The Peltier module and its regulation have not been modelled directly but indirectly through the boundary conditions.

The skin surface area is not cooled directly by the Peltier module because of the difficulties in implementing the thermocouple inside the Peltier module for the temperature regulation. For this reason we used a metal disc, which is in direct contact with the skin and cooled by the Peltier module. The metal disc acts like a heat absorber storing the heat from the skin and regulating the cooling temperature during the cooling process. Using a metal disc can also help to implement the thermocouple for measurement and regulation, for which different thermocouple locations were tested. Weak passive cooling with a metal disc made of brass was used by Strąkowska et al. [42, 44] to locally cool down the skin by $2 - 7°C$. The metal disc has been cooled down to $20 - 23°C$ and then put on the skin for $5s$. This technique does not provide a constant temperature cooling because there is no heat dissipation from the disc. Cooling device in this paper is designed for longer cooling achieving deeper cooling penetration and higher thermal contrast during the recovery phase. The cooling device is active due to the Peltier module, which cools down the metal disc to the desired temperature and keep it at a temperature as constant as possible during the cooling process.

This section covers a detailed description of the computational domain, the mathematical models of bioheat transfer and heat conduction through the disc, local thermoregulation response of the tissue, boundary conditions and temperature regulation to evaluate the cooling device design. The evaluation is done by analysing the simulation results of the DTI cooling process, and which design parameters are most important for constant cooling temperature.

2.1 Computational domain

To simulate the cooling process of DTI using a Peltier cooling device, it is necessary to simulate bioheat transfer in skin tissue with melanoma, as well as heat transfer in metal disc. The Peltier module has not been modelled directly. It was included through boundary conditions on the disc surface as shown in Figure 2. Therefore, the computational domain consists of skin tissue composed of different layers (epidermis, papillary dermis, reticular dermis, fat, muscle and melanoma lesion) and metal disc, and is presented in Figure 1.

The geometric data for the computational domain has been gathered in Table 1 together with lesion sizes. As can be seen from Table 1, the size of the computational domain for skin tissue has been chosen to be $D_t = 100mm$, and the total height is $H_t = 11.6mm$. Based on preliminary results the domain is large enough for the side boundary condition not affecting the solution [39, 43]. For the metal disc, the diameter has been chosen regarding the size of

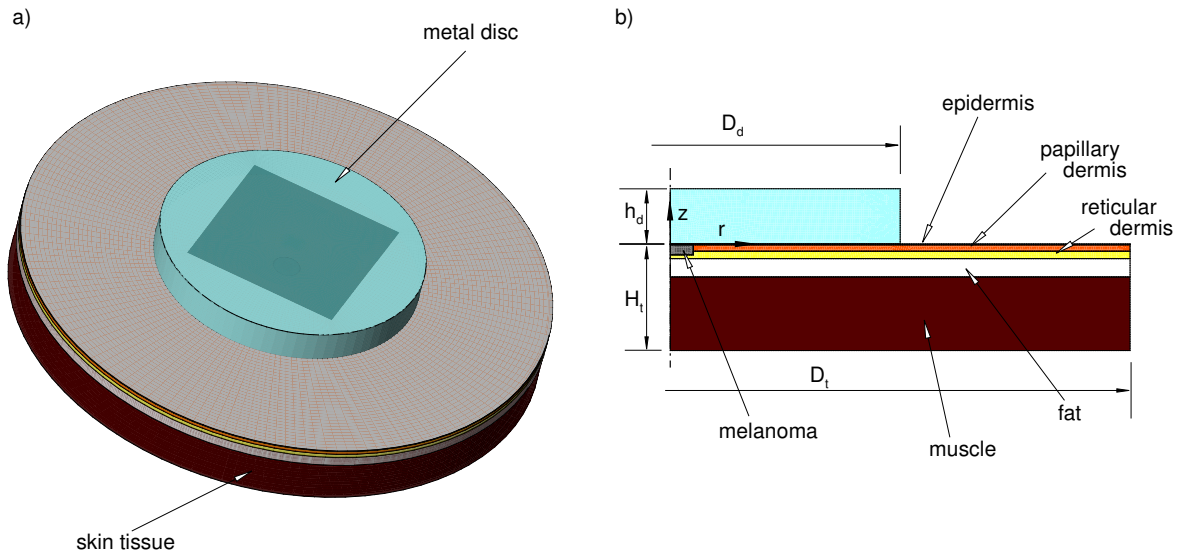

Figure 1: Computational domain of the numerical model including skin tissue and metal disc: a) isometric view and b) cross-sectional view with annotation.

the Peltier module Quick-Cool QC-71-1.4-8.5 ($30mm \times 30mm$) and is $D_d = 50mm$, while the height has been varied from $h_d = 1mm$ to $h_d = 12mm$ in increments of $1mm$ to test the effect of disc thickness, which corresponds to higher thermal capacity. Also, to test the cooling approach, we choose three different melanoma sizes approximated by a cylinder [37, 43, 45], one for Clark II and two for Clark IV. The Clark II melanoma ($h = 0.44mm$, $d = 2mm$) protrudes into the papillary dermis and represents early stage, while the Clark IV ($h = 1.1mm$, $d = 2.5mm$ and $d = 5mm$) protrudes into the reticular dermis and represents advanced stage [1]. Because the Clark IV lesion reflects a higher temperature difference on the skin surface due to higher heat generation and size, we choose two different diameters to test the effect of melanoma size on the achieved cooling temperature.

2.2 Mathematical model

To simulate heat transfer in a metal disc and skin tissue with the aim to evaluate the cooling approach, appropriate governing equations have to be used. Heat transfer in biological tissue has been described by the Pennes bioheat model [46] that has been used for each layer of the tissue. This model is widely accepted [21, 36, 37, 45, 47–49], and is written as:

$$\rho_i c_{p,i} \frac{\partial T}{\partial t} = \vec{\nabla} \cdot \left(\lambda_i \vec{\nabla} T \right) + \omega_{b,i} \rho_b c_{p,b} \left(T_a - T \right) + q_{m,i}, \tag{1}$$

where $T = T(\vec{r}, t)$ represents temperature, ρ_i, λ_i and $c_{p,i}$ are the effective density, thermal conductivity and specific heat of the tissue, respectively, $\omega_{b,i}$ is blood perfusion rate of the tissue, ρ_b blood density, $c_{p,b}$ is specific heat of the blood, T_a is arterial blood temperature, t time, $q_{m,i}$ tissue metabolic heat source and index i tissue layer. The blood perfusion rate is a scalar representing the volumetric blood flow rate per volume of tissue through small arterioles and capillary bed (thermally significant vessels). Pennes assumed that heat transfer

between the blood flow and surrounding tissue happens on the capillary level due to the large interfacial area, therefore, the blood perfusion term acts like a heat source or sink depending on the temperature difference between the tissue and arterial blood flow. During the cooling process of DTI blood perfusion acts like a heat source, heating up the tissue during thermal recovery similar to the metabolic heat source which depends on cell activity. Between these two effects, blood perfusion plays a major role in reheating the tissue [38,43]. Reheating rate not only depends on the blood perfusion rate or metabolic heat source but also on the tissue properties. Therefore, the difference in blood perfusion rate, metabolic heat generation and tissue properties is reflected in the different reheating rates and temperature contrast during the DTI [6, 9, 23].

Parameters in the Pennes model are usually evaluated and treated as constant due to the lack of accurate mathematical models to describe the changing mechanism, as well as due to the large deviation of parameter values which are usually chosen as average values [45, 50, 51]. Therefore, sometimes it is hard to simulate bioheat transfer realistically. In our previous papers [39, 43] we introduced a new approach to model DTI including a local thermoregulation response of blood perfusion rate and metabolic heat generation using the van't Hoff effect [49, 51–58] to simulate DTI more accurately. However, metabolic heat generation has low sensitivity [3, 39, 43], which means that it does not have a high impact on the simulated temperature difference as the blood perfusion rate, and for this reason it has been kept as constant together with other parameters. The blood perfusion rate of the tissue has been modelled as temperature dependent with the following model:

$$\omega_{b,i}\left(T\right) = \omega_{b,i,bas} Q_{10}^{\left(\frac{T-T_0}{10}\right)}, \tag{2}$$

where Q_{10} represents the blood perfusion rate coefficient, $\omega_{b,i,bas}$ represents the basal blood perfusion rate of the tissue and T_0 is the equilibrium temperature of the body.

To model heat transfer in a metal disc, a model for conservation of energy has been used as:

$$\rho_d c_{p,d} \frac{\partial T}{\partial t} = \vec{\nabla} \cdot \left(\lambda_d \vec{\nabla} T\right), \tag{3}$$

where only accumulation and diffusion play a major role in heat transfer. While in equation (1) density, specific heat and thermal conductivity represent material properties for tissue, now these properties belong to the metal disc (copper) annotated by index d. As can be seen comparing equations (1) and (3), there is no heat source or sink in the metal disc which is cooled by the Peltier module included in the numerical simulation through boundary conditions presented in the next subsection.

The material properties for tissue have been taken from [21, 37, 39, 45], and have been treated as constant for each tissue, same as the properties for the metal disc (copper), which have been taken from engineering tables [59]. The exception is blood perfusion rate, which is temperature dependent. All material properties are gathered in Table 1 together with the dimensions of the computational domain. For the Q_{10} coefficient, values have been taken according to [43], as $Q_{10} = 1.1$ for melanoma lesion and $Q_{10} = 2.0$ for healthy tissue.

2.3 Boundary conditions

To simulate the cooling process of the skin using the designed cooling device, we have to prescribe appropriate initial and boundary conditions for the whole computational domain.

Material	$d[mm]$	$h[mm]$	$\rho[kg/m^3]$	$c_p[J/kgk]$	$\lambda[W/mK]$	$\omega_{b,bas}[1/s]$	$q_m[W/m^3]$
epidermis	100.0	0.1	1200	3589	0.235	0.0	0.0
papillary dermis	100.0	0.7	1200	3300	0.445	0.0002	368.1
reticular dermis	100.0	0.8	1200	3300	0.445	0.0013	368.1
fat	100.0	2.0	1000	2674	0.185	0.0001	368.3
muscle	100.0	8.0	1085	3800	0.510	0.0027	684.2
Clark II	2.0	0.44	1030	3852	0.558	0.0063	3680
Clark IV	2.5,5.0	1.1	1030	3852	0.558	0.0063	3680
blood	–	–	1060	3770	–	–	–
copper disc	50.0	1.0-12.0	8960	390	399	–	–

Table 1: Material properties and dimensions.

The boundary conditions for the tissue are taken from [21,37,39,45]. Figure 2 shows different surfaces on which we prescribed different boundary conditions together with their annotation. For the bottom part, we prescribe constant body core temperature $T_0 = 37.0°C$, which is the mean value for a healthy person in a resting position. On the sides of the computational domain, we prescribe adiabatic boundary condition ($q = 0$) assuming that the diameter D_t of the computational domain is large enough not to affect the computational solution. At the skin and the metal disc surface we have to prescribe the heat transfer between the part and the surrounding environment, which has been modeled with a Robin boundary condition using $\alpha = 10W/m^2K$ and $T_\infty = 22.0°C$.

For the Peltier surface, where the Peltier module is attached, we prescribed a heat flux that has been calculated dynamically through time regarding the regulation and the difference between the thermocouple measurement T_m and the preset cooling temperature T_{set}. In

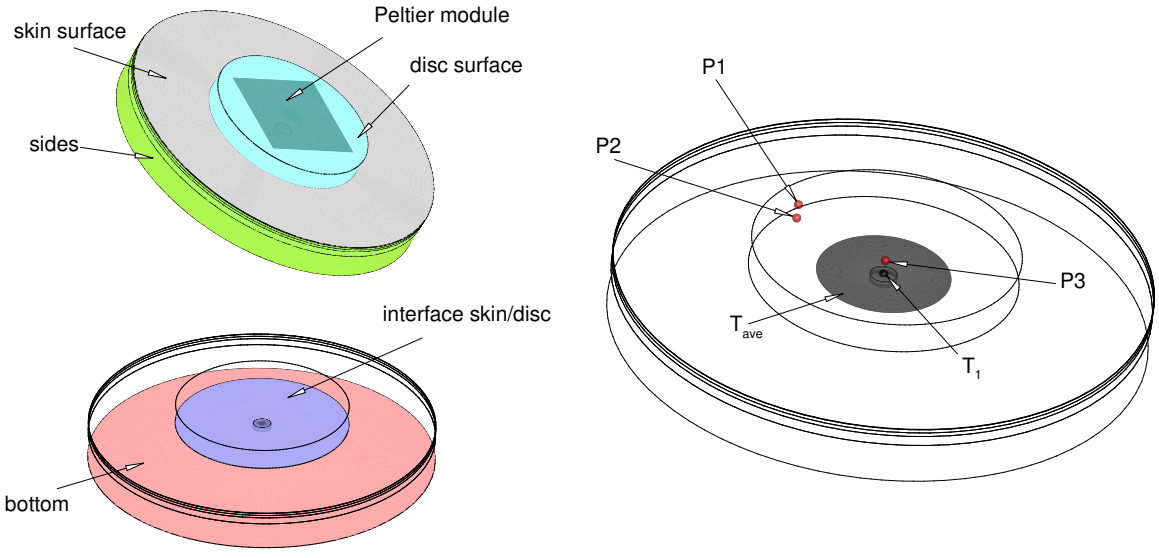

Figure 2: Position of different boundary conditions, their annotation and position of the temperature measurement.

this paper, we investigated how the thermocouple position shown in Figure 2 affects the regulation and the achieved cooling temperature. Therefore, four different cases have been tested: the first is when the temperature measurement is taken at position P1 $\vec{r} = (3/8D_d, h_d)$, the second at position P2 $\vec{r} = (3/8D_d, h_d/2)$, the third at position P3 $\vec{r} = (0.0, h_d/2)$ and the fourth represents the average measurement of positions P1 and P3. The position of points is written in accordance to the polar coordinate system $\vec{r} = \vec{r}(r, z)$, which is shown in Figure 1. Regarding the temperature difference between the measured temperature and the preset temperature, a current applied to the Peltier module has been calculated as:

$$I(t) = \mu (T_m - T_{set}), \tag{4}$$

where I represents the current, μ linear coefficient and T_m and T_{set} temperature measurement and preset temperature, respectively. Here, we tested different values of μ from $\mu = 1.0A/K$ to $\mu = 10.0A/K$ in increments of $1.0A/K$. According to the current applied to the Peltier module, the generated heat flow has been calculated by a fourth order polynomial equation:

$$Q(t) = a_1 I^4(t) + a_2 I^3(t) + a_3 I^2(t) + a_4 I(t), \tag{5}$$

where the polynomial coefficients are $a_1 = 0.0073W/A^4$, $a_2 = -0.1516W/A^3$, $a_3 = 0.6945W/A^2$ and $a_4 = 4.9422W/A$. The polynomial equation (5) has been extracted by interpolating data provided by the manufacturer. Figure 3 shows the heat flow by the Peltier module Quick-Cool QC-71-1.4-8.5 depending on the applied current and achieved temperature difference, together with the extrapolated polynomial equation (5). The temperature difference between the cold and hot sides has been taken as $\Delta T = T_{set} - T_\infty$, assuming that the temperature on the hot side is equal to the ambient temperature T_∞ and that, on the cold side, the preset cooling temperature T_{set} is achieved. Of course, this cannot

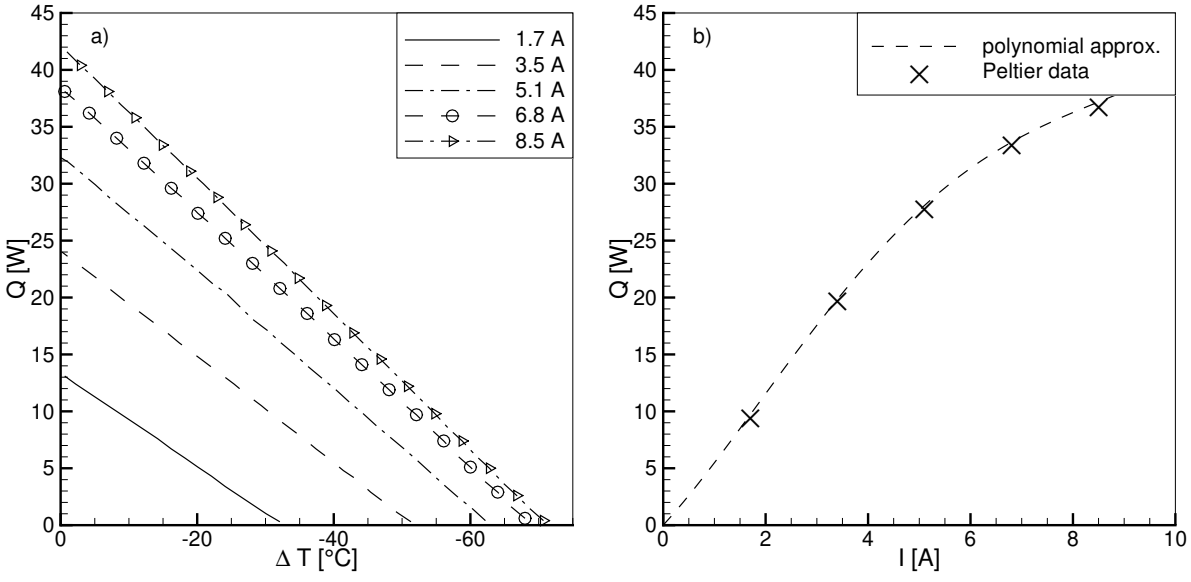

Figure 3: Heat flow according to the manufacturer data regarding the temperature difference between cold and hot sides and current a) and extrapolated polynomial function for the temperature difference $\Delta T = -9.0°C$ b).

be met in a real experimental test because the difference between the cold and hot sides will change; however, for numerical evaluation of different designs, this assumption will not affect the conclusions. The device design has been tested for the preset cooling temperature $T_{set} = 13.0°C$ [3, 37, 43] that produces better temperature contrast in melanoma screening and deep cooling penetration [21]. Therefore, the temperature difference is $\Delta T = -9.0°C$ and kept as constant. Regarding the prescribed boundary condition on the Peltier surface, we prescribed the heat flux, which has been calculated as:

$$q\left(t\right) = \frac{Q\left(t\right)}{A}, \tag{6}$$

where A represents the surface area of the Peltier element of dimension $A = 9 \cdot 10^{-4} m^2$.

At the interfaces between different tissue layers, we also have to impose equilibrium $\lambda_l \partial T_l / \partial \vec{n}_l = -\lambda_{l+1} \partial T_{l+1} / \partial \vec{n}_{l+1}$ and compatibility conditions $T_l = T_{l+1}$, where $\vec{n}$ represents the normal on the interface boundary and indices l and $l+1$ represent adjoining tissues. The only non-compatibility condition has been imposed on the interface between the skin and metal disc, where the contact thermal resistance has been included as:

$$T_s = T_d + \left(\vec{q} \cdot \vec{n}_s\right) R \tag{7}$$

where T_s represents skin temperature, T_d temperature of the metal disc on the interface, $\vec{q}$ is interface heat flux, $\vec{n}_s$ normal vector of the skin domain and R the contact thermal resistance. The equilibrium condition is still met for the contact surface between skin and metal disc; $\vec{q} = \vec{q}_s = \vec{q}_d$. The value of the thermal resistance between metal disc and skin has been chosen according to [60] and was taken as $R = 0.001 m^2 K/W$, that represents good thermal contact.

For the initial temperature condition $T(t = 0)$ of the skin tissue, we prescribed the steady-state solution of the bioheat problem determined with the described boundary conditions on the bottom part, sides and skin surface without the metal disc, while for the computational domain of the disc we prescribed the preset temperature T_{set} to which the cooling device is cooled. Numerical simulation to assess the cooling design has been done for the cooling time of $\tau = 60s$ [21, 37, 39, 45].

3 Boundary Element Method

To solve the numerical model and to simulate the cooling process using the previously described cooling device, the subdomain BEM approach has been used. The main reason for choosing this method is its advanced treatment of boundary conditions that improves the accuracy of the numerical method, and the increased computational speed due to the subdomain approach [43, 61]. In this paper, as we are dealing with a full 3D geometry and a non-linear governing equation (1) due to the temperature-dependent blood perfusion. A short derivation of the BEM numerical scheme based on the elliptic fundamental solution to solve heat transfer problems will be shown in this section.

The governing equations (1) and (3) written for each subdomain or tissue layer has been treated in the form of a Poisson equation:

$$\vec{\nabla}^2 u(\vec{r}) = b(\vec{r}), \tag{8}$$

where $\vec{\nabla}^2$ represents the Laplace operator, $u(\vec{r})$ is an arbitrary field function, $b(\vec{r})$ is the source term or the non-homogeneous part of the equation and $\vec{r} = \vec{r}\,(x, y, z)$ is an arbitrary spatial vector. We start with the integral form of Green's second identity, which for the Poisson equation (8) is written in the form:

$$c(\vec{\xi})u(\vec{\xi}) = \int_{\Gamma} \vec{q}(\vec{R})u^*(\vec{\xi}, \vec{R})d\vec{\Gamma} - \int_{\Gamma} u(\vec{R})\vec{q^*}(\vec{\xi}, \vec{R})d\vec{\Gamma} - \int_{\Omega} b(\vec{r})u^*(\vec{\xi}, \vec{r})d\Omega, \tag{9}$$

where Ω and Γ represent the domain and boundary, respectively, $\vec{R} = \vec{R}\,(x, y, z)$ is the spatial vector of the boundary, $\vec{q} = \partial u/\partial\vec{n}$ is the normal derivative of the field function u, $\vec{\xi} = \vec{\xi}\,(x, y, z)$ represents the position of the source point, $c(\vec{\xi})$ the free coefficient that depends on the position of the source point, and $u^*(\vec{\xi}, \vec{R})$ and $\vec{q^*}(\vec{\xi}, \vec{R}) = \partial u^*(\vec{\xi}, \vec{R})/\partial\vec{n}$ are the fundamental solution and its normal derivative, respectively.

The elliptic fundamental solution for a 3D computational domain is given by the equation:

$$u^*(\vec{\xi}, \vec{r}) = \frac{1}{4\pi d(\vec{\xi}, \vec{r})}, \tag{10}$$

where $d(\vec{\xi}, \vec{r})$ represents the distance between source and field points:

$$d = d(\vec{\xi}, \vec{r}) = \sqrt{(x_\xi - x_p)^2 + (y_\xi - y_p)^2 + (z_\xi - z_p)^2}, \tag{11}$$

where the source point is defined by coordinates $\vec{\xi} = \vec{\xi}(x_\xi, y_\xi, z_\xi)$ and the field point by $\vec{r} = \vec{r}(x_p, y_p, z_p)$. The normal derivative of the fundamental solution is defined by the equation:

$$q^*(\vec{\xi}, \vec{R}) = -\frac{(x_\xi - x_p)}{4\pi d^3}n_x - \frac{(y_\xi - y_p)}{4\pi d^3}n_y - \frac{(z_\xi - z_p)}{4\pi d^3}n_z, \tag{12}$$

where n_x, n_y and n_z represent the components of the normal vector on the boundary $\vec{n}(\vec{R}) = \{n_x, n_y, n_z\}$.

The value of the free coefficient $c(\vec{\xi})$ depends on the position of the source point $\vec{\xi}$ and is defined as:

$$\begin{array}{ll} c(\xi) = 1, & \vec{\xi} \in \Omega, \\ c(\xi) = \beta/(4\pi), & \vec{\xi} \in \Gamma. \end{array} \tag{13}$$

where β represents the internal angle of the boundary at point $\vec{\xi}$.

Eight-node linear cells (hexahedron) have been used for geometry discretisation, and consequently four-node linear elements (quadrilateral) for the boundary. For the approximation of the field function $u(\vec{r})$ and non-homogeneous part $b(\vec{r})$, quadratic interpolation functions have been used with constant interpolation for the normal derivative on the boundary $q(\vec{R}) = \partial u(\vec{R})/\partial n$. The representative element used in the subdomain approach is shown in Figure 4, together with the position of the interpolation nodes.

Applying expression (9) at every computational node of each cell separately, we obtain a global system of equations for the Poisson equation (8) which can be written as:

$$[H]\{u\} = [G]\{q\} - [S]\{b\}, \tag{14}$$

where $[H]$, $[G]$ and $[S]$ are the matrices, $\{u\}$ is the vector of discrete values of the field function, $\{q\}$ is the vector of discrete values of the normal derivative of u and $\{b\}$ is the

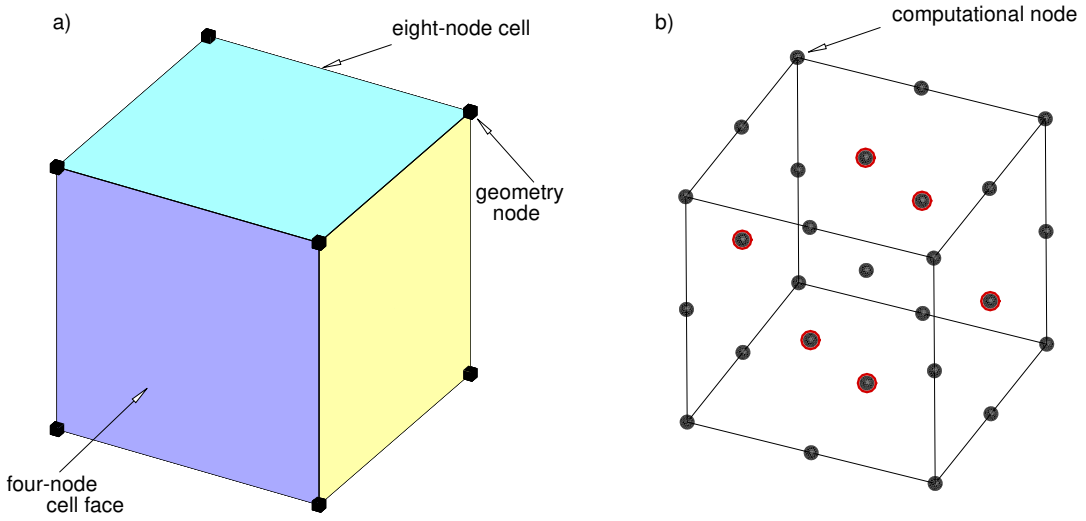

Figure 4: Representation of the mesh cell used in BEM a) and position of the interpolation nodes (black spheres represent computational nodes for the field function u while circled ones for the normal derivative q).

vector of discrete values of the non-homogeneous part. A more detailed description of the matrix coefficients can be found in our previous work [61].

We can now apply the above procedure to the bio-heat equation (1), where at first we rewrite the equation in the form of the Poisson equation (8):

$$\vec{\nabla}^2 T = \frac{1}{a_{diff}} \frac{\partial T}{\partial t} - \frac{\omega_b \left(T\right) \rho_b c_{p,b}}{\lambda} \cdot \left(T_a - T\right) - \frac{q_m}{\lambda}, \tag{15}$$

where $a_{diff} = \lambda / \rho c_p$ represents the thermal diffusivity and $\omega_b \left(T\right)$ is a temperature-dependent parameter. The non-homogeneous part $b(\vec{r})$ is now:

$$b(\vec{r}) = \frac{1}{a_{diff}} \frac{\partial T}{\partial t} - \frac{\omega_b \left(T\right) \rho_b c_{p,b}}{\lambda} \cdot \left(T_a - T\right) - \frac{q_m}{\lambda}. \tag{16}$$

The time derivative of the temperature is estimated by the second-order finite diference (FD) scheme [61] as:

$$\frac{\partial T}{\partial t} \approx \frac{3T^t - 4T^{t-1} + T^{t-2}}{2\Delta t}, \tag{17}$$

where superscript indices t, $t-1$ and $t-2$ represent different time steps and Δt is the time difference between two adjacent time steps. For the first time step, the following assumption has been made; $T^{t-1} = T^{t-2}$, which reduces the FD time marching scheme to first-order. Including the approximation (17) into equation (15) and using a fully implicit scheme ($T = T^t$, $q = q^t$), the global system of equations (14) can be rewritten as:

$$\left([H] + \left\{ \frac{3}{2a_{diff}\Delta t} + \frac{\omega_b \left(T^t\right) \rho_b c_{p,b}}{\lambda} \right\} [S] \right) \left\{T^t\right\} = [G] \left\{q^t\right\} + \left\{ \frac{2}{a_{diff}\Delta t} \right\} [S] \left\{T^{t-1}\right\}$$

$$-\left\{\frac{1}{2a_{diff}\Delta t}\right\}[S]\left\{T^{t-2}\right\}+[S]\left\{\frac{\omega_b\left(T^t\right)\rho_b c_{p,b}}{\lambda}T_a+\frac{q_m}{\lambda}\right\}. \tag{18}$$

The system of equations (18) is non-linear and has to be solved using a non-linear iteration solver within each time step. Therefore, the final form of equation (18) is

$$\left([H]+\left\{\frac{3}{2a_{diff}\Delta t}+\frac{\omega_b\left(T_{k-1}^t\right)\rho_b c_{p,b}}{\lambda}\right\}[S]\right)\left\{T_k^t\right\}=[G]\left\{q^t\right\}+\left\{\frac{2}{a_{diff}\Delta t}\right\}[S]\left\{T^{t-1}\right\}$$
$$-\left\{\frac{1}{2a_{diff}\Delta t}\right\}[S]\left\{T^{t-2}\right\}+[S]\left\{\frac{\omega_b\left(T_{k-1}^t\right)\rho_b c_{p,b}}{\lambda}T_a+\frac{q_m}{\lambda}\right\}. \tag{19}$$

where indices k and $k-1$ represent the current and previous non-linear iteration steps, respectively. The non-linear loop is controlled by the maximum number of steps and the RMS (Root Mean Square) error as:

$$k>k_{max}, \qquad \varepsilon_{RMS,k}\leq\varepsilon_{max}, \tag{20}$$

where k_{max} represents the maximum number of non-linear steps, ε_{RMS} the RMS error and ε_{max} the maximum error. The RMS error is calculated at every iteration step as:

$$\varepsilon_{RMS,k}=\sqrt{\frac{1}{n}\sum_{i=1}^{n}\frac{\left(T_{i,k-1}-T_{i,k}\right)^2}{T_{i,k}^2}}, \tag{21}$$

where index i represents the computational node and n the total number of nodes in the computational domain. When convergence of the non-linear loop is achieved, meaning the RMS error is lower than the prescribed maximum or the maximum number of steps is reached, the non-linear iteration is stopped and the calculation for a new time step can begin.

The non-linear system of equations (19) is used to solve the heat transfer problem in the tissue domain; however, to simulate heat transfer in the metal disc, we also have to discretise equation (3). Rewriting equation (3) into Poisson form (8) we obtain:

$$\vec{\nabla}^2 T=\frac{1}{a_{diff}}\frac{\partial T}{\partial t}, \tag{22}$$

where the non-homogeneous part $b(\vec{r})$ is now:

$$b(\vec{r})=\frac{1}{a_{diff}}\frac{\partial T}{\partial t}. \tag{23}$$

Applying the FD scheme for the time derivative (17) into equation (23) and using a fully implicit scheme as before, we can rewrite the global system of equations (14) derived for the Poisson equation as:

$$\left([H]+\left\{\frac{3}{2a_{diff}\Delta t}\right\}[S]\right)\left\{T^t\right\}=[G]\left\{q^t\right\}+\left\{\frac{2}{a_{diff}\Delta t}\right\}[S]\left\{T^{t-1}\right\}$$
$$-\left\{\frac{1}{2a_{diff}\Delta t}\right\}[S]\left\{T^{t-2}\right\}, \tag{24}$$

where we obtain a linear system of equations that can be solved only once.

The non-linear system of equations (19) and (24) represent the BEM numerical scheme for solving heat transfer problems inside skin tissue with temperature-dependent blood perfusion, and inside the metal disc. By applying the boundary and interface conditions, the system of equations can be rewritten as a global system of linear equations and solved using a standard solver. We used FORTRAN coding to implement and test the proposed BEM scheme, as already done in our previous work [43, 61, 62]. The result is the temperature field for the whole computational domain and the normal derivative of the temperature on the boundary. From our previous experience, we find this approach suitable for solving complicated non-linear problems achieving good numerical accuracy and fast computational time [61, 62].

4 Results and discussion

In this paper, we are numerically testing the design of a device for constant temperature cooling at DTI, using a metal disc and a Peltier module for active cooling. Prior to manufacturing the device and experimental setup, we would like to evaluate the most important parameters to achieve constant cooling. Therefore, different versions were analysed by changing the position of the thermocouple for the Peltier regulation, disc thickness, regulation coefficient μ, as well as the effect of the lesion size, to determine the most appropriate version.

Based on our previous work [39, 43, 61] where representative element size of $\Delta\ell = 0.5mm$ for tumour discretisation and time step $\Delta t = 1s$ were shown to be sufficient, we chose element size of $\Delta\ell = 0.1mm$ for tumour discretisation and time step of $\Delta t = 0.1s$. For domain discretisation, a structured mesh has been used as shown in Figure 5, where the minimal number of elements in z direction of the layer was 3. The number of elements is $258,240$ while the number of computational nodes is $1,134,794$, which is sufficient to produce

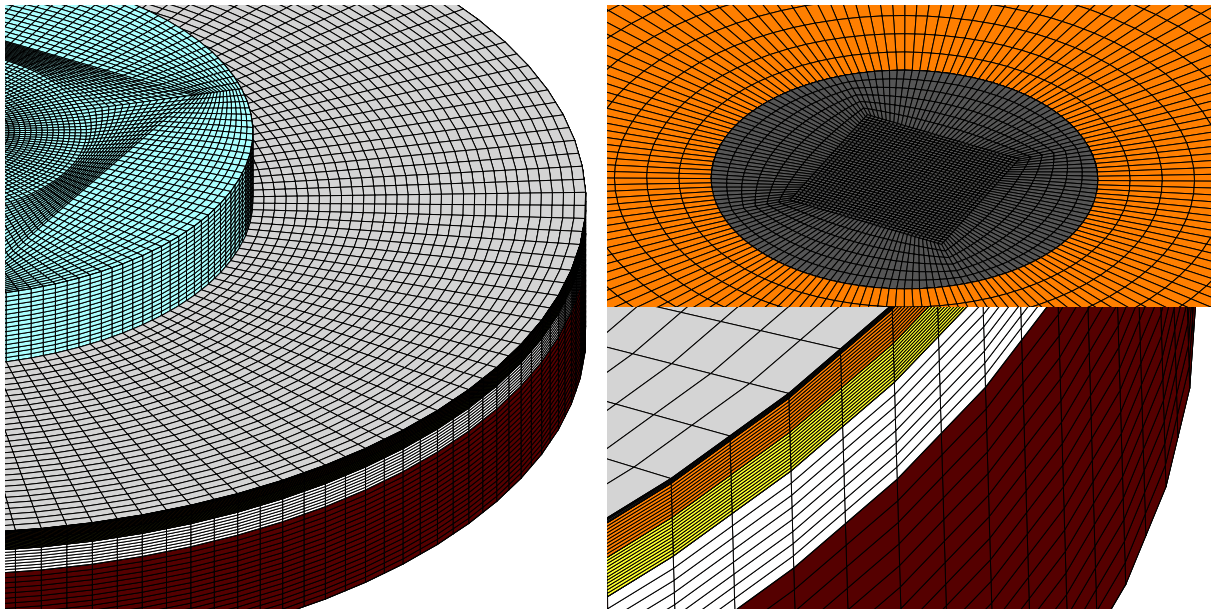

Figure 5: Computational mesh with detailed presentation of the structured mesh.

mesh independent results. With the time step of $\Delta t = 0.1s$, which is sufficient for the elliptic fundamental solution as shown in [61], the number of time steps was 600 to simulate the cooling period of $\tau = 60s$. Because the focus of the paper is to represent the results and conclusion for the active cooling device, the mesh and time step analysis is omitted in this paper.

For design evaluation, we observed the average temperature on the skin surface in the radius $R = 12.5mm$ from the centre (T_{ave}), as well as the temperature in the centre (T_1), as shown in Figure 2. The objective is to achieve constant temperature T_{ave} and T_1 during the cooling process and close to the preset temperature T_{set}. In the following subsections, the results of various configurations are presented, plotting the transient cooling temperature on the skin surface, as well as the evaluation of the temperature difference between the preset and achieved cooling temperature is made.

To analyse how thermocouple position, regulation coefficient μ, disc thickness h_d and tumour size affect the device design, a total of 138 simulations has been done. For clarity, table 2 shows the number of simulations n_{sim} done for this analysis together with the description. The analyses have been done in three parts, first is analysing the thermocouple position, second was to analyse the disc thickness and regulation coefficient and the last part was to analyse the lesion size. The simulations have been run on an Intel Core i9-7900X (3.30GHz) processor in serial and took $39.33h$ of CPU time for each simulation. To save on time, we run simulations on multiple computers.

First part - Clark II					n_{sim}
thermocouple position	P1	P2	P3	(P1+P3)/2	16
h_d	$3mm$		$9mm$		
μ	$1A/K$		$4A/K$		
Second part - Clark II and thermocouple P1					n_{sim}
h_d	$1mm - 12mm$				120
μ	$1A/K - 10A/K$				
Third part - thermocouple P1 and $h_d = 3mm$					n_{sim}
case	healthy skin	Clark II	Clark IV $2.5mm$	Clark IV $5mm$	8
μ	4A/K		8A/K		

Table 2: Number of simulation runs with description.

4.1 Position of the thermocouple

Four different cases compare how the position of the temperature measurement or thermocouple position for Peltier regulation affects the skin cooling temperature. The first case is when the temperature measurement is taken on the surface of the metal disc near the edge (P1), the second is below point P1 in the middle of the disc thickness (P2), the third is in the middle of the disc thickness below the Peltier module and in the centre (P3), and the last one is the average measurement from positions P1 and P3, as shown in Figure 2.

Figure 6 shows the average temperature on the skin surface T_{ave} comparing all four cases, for disc thickness of $h_d = 3mm$ and $h_d = 9mm$, and for two different regulation coefficients $\mu = 1A/K$ and $\mu = 4A/K$, where we can conclude that there is no difference between the first and second cases while the difference between the achieved cooling temperature

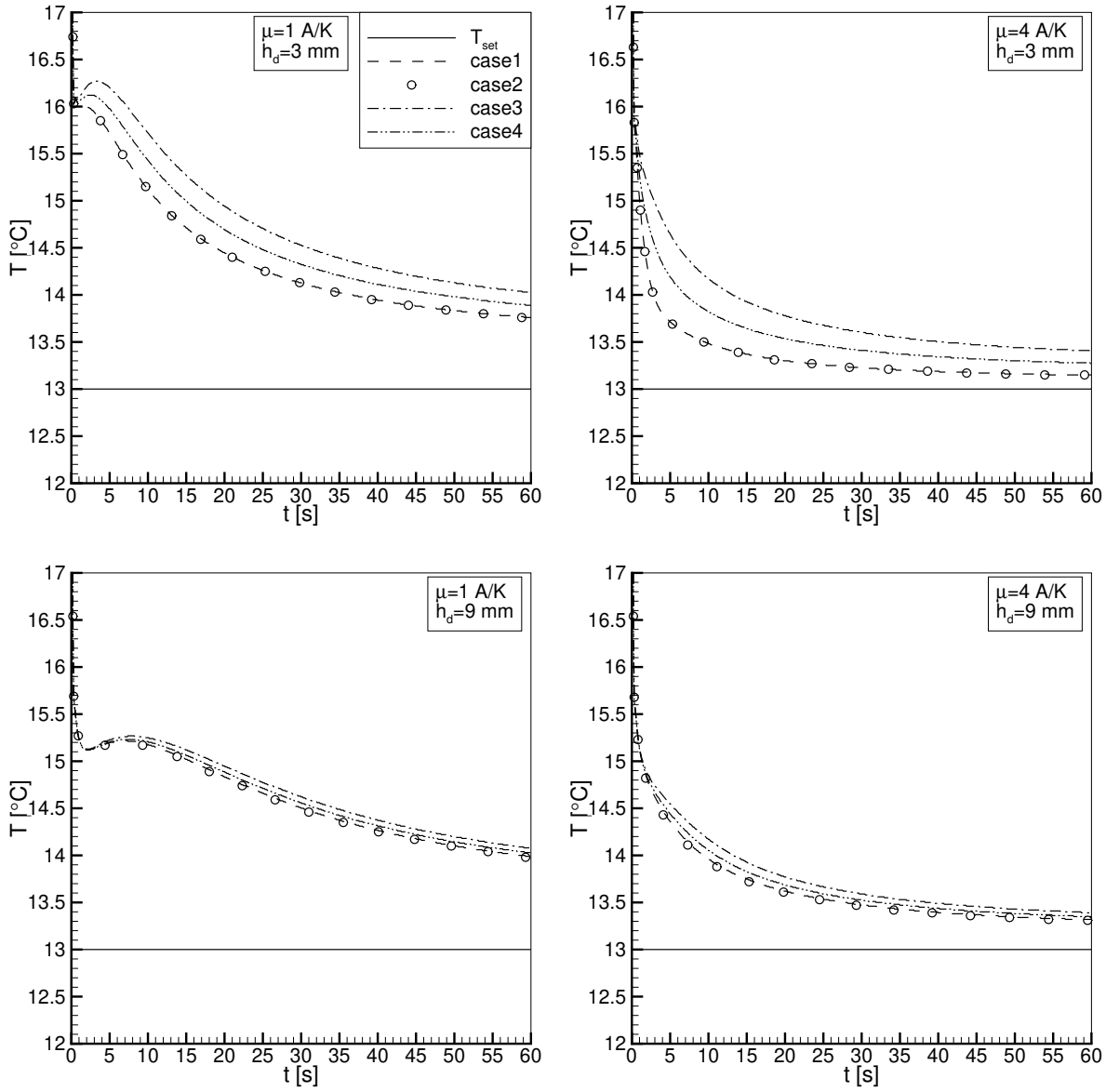

Figure 6: Transient average temperature T_{ave} for different disc thickness h_d and regulation coefficient μ depending on the position of temperature measurement.

becomes smaller with increasing disc thickness, and more independent of the position of temperature measurement. We can also observe that the lowest cooling temperature is achieved at thermocouple position P1 or P2, and the highest from the centre of the disc (P3). However, when the average temperature measurement is taken for regulation, the cool-down temperature lies between the first and third cases, which is to be expected. The reason for lower cooling temperature for thermocouple position P1 or P3 is in the delay between the system response and Peltier cooling, due to the heat conduction inside the disc in the radial direction, and therefore lower skin temperature during the cooling. The cooling temperature drops from the steady-state skin temperature, which is around $34.5°C$, to a range of $15.0 - 16.0°C$ because of the cooling capacity of the metal disc that is pre-cooled

to 13.0°C. After that, the cooling process with the Peltier module takes place, which is especially visible for $\mu = 1A/K$. Using a low value of μ, the response of the cooling device is slow and does not cool down the skin tissue to the desired temperature. After 60s of cooling, it reaches a temperature of 14.0°C. However, by increasing the regulation value μ, cooling is much quicker due to the higher heat flux on the Peltier module, dropping the temperature close to the desired value of 13.0°C.

From this, we can conclude that the position of temperature measurement is not very important for thicker discs, however lower cooling temperatures are achieved using temperature measurement from location P1, which is also easier to implement than in the centre of the disc, and is preferred. One reason for this expected behavior can be found in the high thermal conductivity of the material. Figure 7 shows a comparison between the average and centre temperature for disc thicknesses $h_d = 3mm$ and $h_d = 9mm$ using thermocouple position P1, from which we can conclude that there is a negligible temperature difference for a thicker disc while, for a thinner disc, there is a small difference, however the shape is the same. Therefore, for the next set of results, we will focus only on the thermocouple position P1, which is most convenient from the practical point of view, and lower cooling temperatures can be achieved.

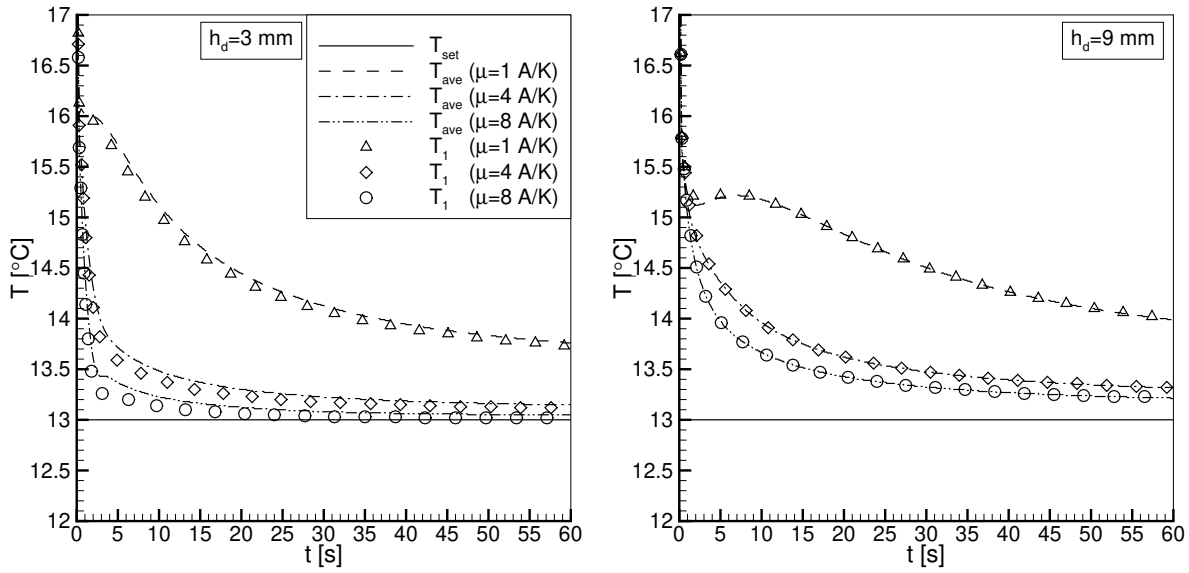

Figure 7: Comparison of average cooling temperature T_{ave} and temperature in the center T_1 for the thermocouple position P1 and different value of regulation coefficient μ and disc thickness h_d.

4.2 Disc thickness and regulation

In this section, we tested different disc thicknesses and values of the regulation coefficient, to determine how it affects the cooling temperature and its shape. Figure 8 shows the average temperature T_{ave} on the skin surface for different disc thicknesses and different values of the regulation coefficient. As can be observed, the regulation response is slower for thicker discs, and also the achieved cooling temperature at the end of the cooling process is

slightly higher for the same value of coefficient μ. The reason for this behavior is the higher thermal capacity of the disc that can absorb greater amounts of heat. Therefore, for the first few seconds we can observe that, for a thicker disc, a lower temperature can be achieved comparing the cooling temperature curves for $\mu = 1A/K$. For a disc thickness of $h_d = 3mm$, the initial cool down temperature is $16.0°C$, while for $h_d = 12mm$ it is slightly below $15.0°C$. However, the initial cool down is better for a thicker disc, the regulation is slower and also the average cooling temperature is slightly higher. The achieved cooling temperature using a high value of μ is somehow similar for disc thicknesses from $h_d = 6mm$ to $h_d = 12mm$, while it is lower for a thin disc. For $h_d = 3mm$ and $\mu = 8A/K$, we can achieve a cooling temperature that is very close to the preset temperature, and from $20s$ to $60s$, it is in the

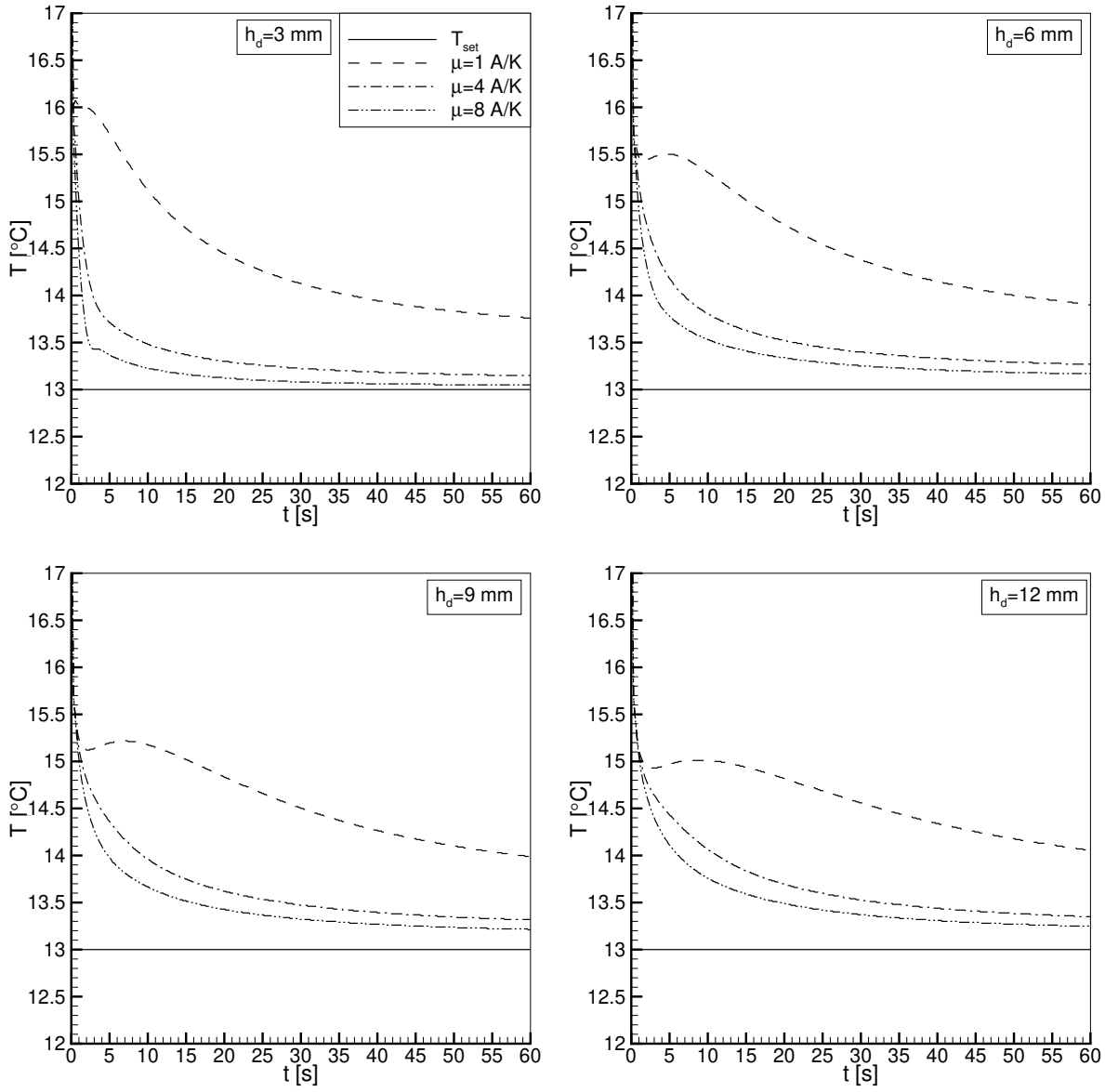

Figure 8: Cooling temperature T_{ave} for different values of the regulation coefficient μ and disc thickness h_d.

range of $13.1°C$ and almost constant. A thin disc does not have a high thermal capacity, for which it heats up quicker with the skin contact and can be measured by the thermocouple. Therefore, regulation or cooling with the Peltier module is more distinct and a lower cooling temperature can be achieved.

Using a disc thickness $h_d = 3mm$, the time averaged cooling temperature is $14.40°C$ for $\mu = 1A/K$, $13.35°C$ for $\mu = 4A/K$ and $13.16°C$ for $\mu = 8A/K$, which is very close to the desired temperature. To conclude, the disc thickness acts like a heat damper, the thicker the disc, the slower the regulation and slightly higher cooling temperature, however we can achieve better initial cooling. One parameter in the design evaluation can therefore be the temperature difference between the average cooling temperature and the preset temperature.

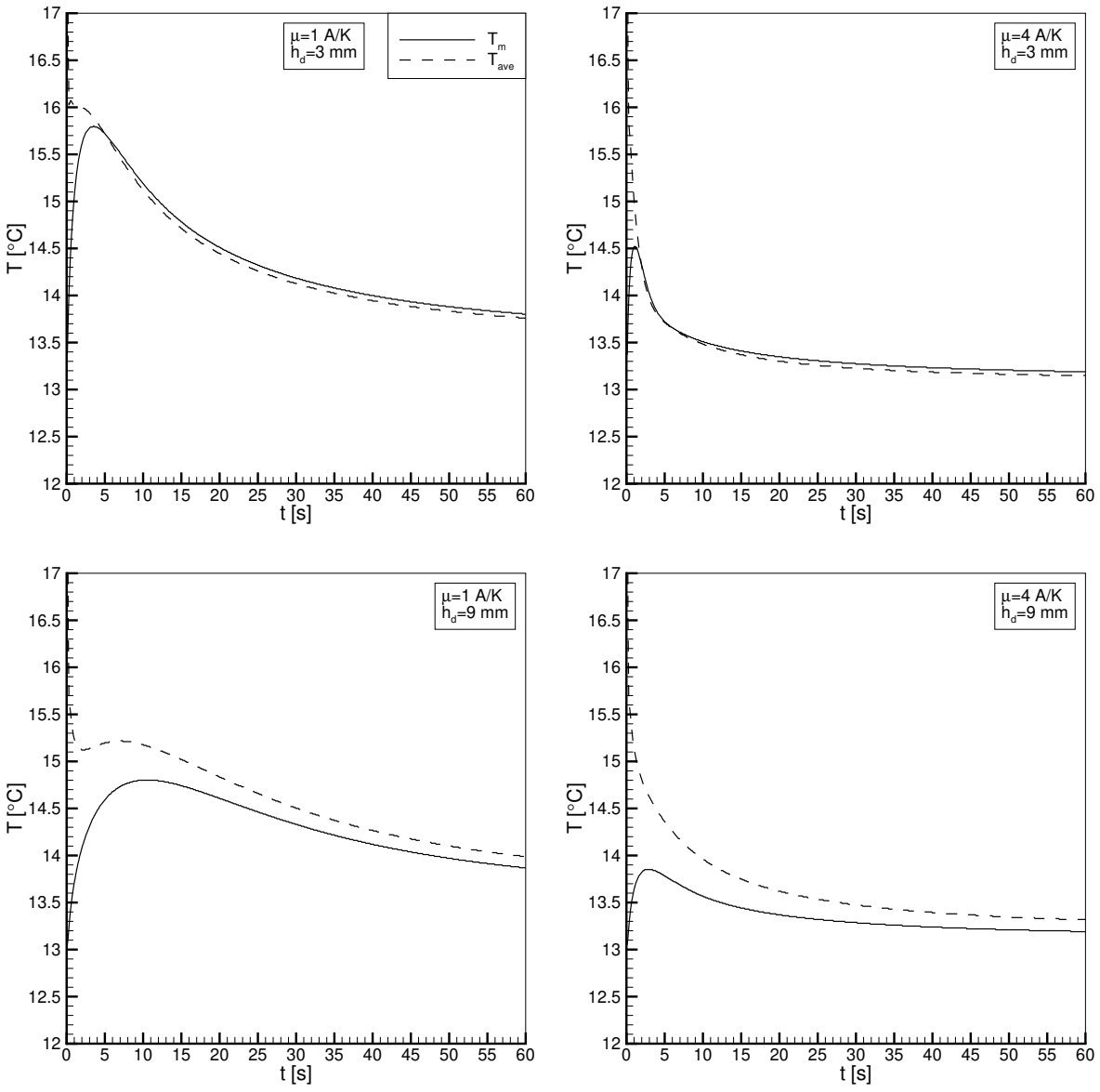

Figure 9: Transient temperature measurement T_m and average cooling temperature T_{ave} for different regulation coefficient μ and disc thickness h_d.

Figure 9 shows the measured temperature by the thermocouple T_m at position P1 and average cooling temperature T_{ave} for different values of μ and disc thickness h_d. As can be observed, the difference between achieved cooling temperature and measurement of the disc temperature in P1 is smaller for a thinner disc than for a thicker one, and also the shape of the temperature measurement depends on the regulation coefficient. The shape of the temperature measurement on the achieved cooling temperature is very similar for a $3mm$ disc, except at the beginning of the process. This can be helpful in determining the actual cooling temperature, that can be evaluated through the measurement of the disc temperature if the temperature difference is small. Therefore, one of the important parameters at design evaluation can also be the temperature difference between the achieved average cooling temperature and the temperature measurement.

The temperature differences $\Delta T_{ave} = T_{ave} - T_{set}$ and $\Delta T_1 = T_1 - T_{set}$, depending on the disc thickness h_d and for different values of the regulation coefficient μ, is shown in Figure 10 together with the temperature difference $\Delta T_{ave,m} = T_{ave} - T_m$, which indicates how the temperature measurement can be used to determine the actual cooling temperature. There is a small difference between ΔT_{ave} and ΔT_1 for thinner discs, indicating less uniform cooling temperature on the skin surface, which has already been observed in Figure 7. Using a thinner disc produces a lower temperature difference ΔT_{ave}, which is preferable from the point of getting closer to the preset temperature, however there will be a temperature non-homogeneity, that can be expressed as $\Delta \bar{T} = \Delta T_1 - \Delta T_{ave}$. Increasing the regulation coefficient μ decreases the temperature difference and can also under-cool the skin in the case of a thin disc and high value of μ. The change of ΔT_{ave} and ΔT_1 is more distinct for the change of μ from $1A/K$ to $4A/K$ than for further increases. Choosing the optimal design or disc thickness depends on the desired non-homogeneity of the cooling temperature and temperature difference ΔT_{ave}, which should be close together and close to zero and can be

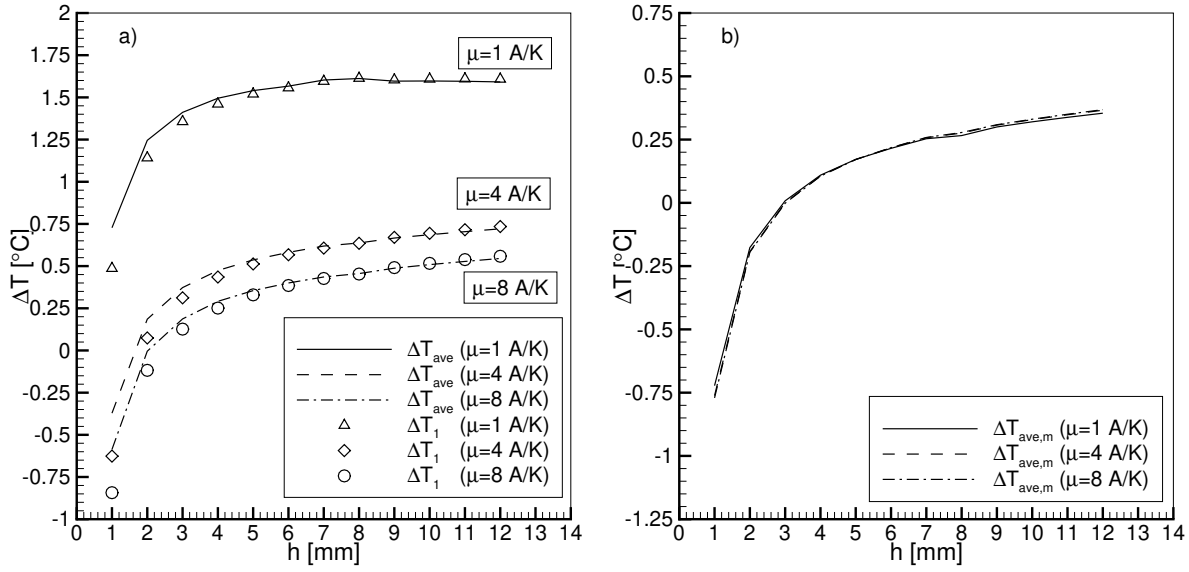

Figure 10: Temperature difference ΔT_{ave} and ΔT_1 depending on the disc thickness h_d and regulation coefficient μ a) and temperature difference $\Delta T_{ave,m}$ showing the difference between the cooling temperature and measured temperature b).

affected by the value of μ. However, changing the coefficient μ does not affect the temperature difference between the measurement and achieved cooling temperature $\Delta T_{ave,m}$ that depends only on the disc thickness, as can be observed in Figure 10.

Figure 11 shows the temperature difference ΔT_{ave}, non-uniformity $\Delta \bar{T}$ and $\Delta T_{ave,m}$ depending on the disc thickness h_d and regulation coefficient μ, for a more clear presentation of the design performance. Values close to zero are coloured green and represent the optimal case. As can be seen, to achieve a cooling temperature that is close to the preset temperature a disc thickness of $h_d = 2mm$ should be considered, however, because of high non-uniformity, a thicker disc is advised. While looking at the $\Delta T_{ave,m}$ there is an optimum range for disc thickness in between $h_d = 2mm$ and $h_d = 4mm$. Taking into account all the

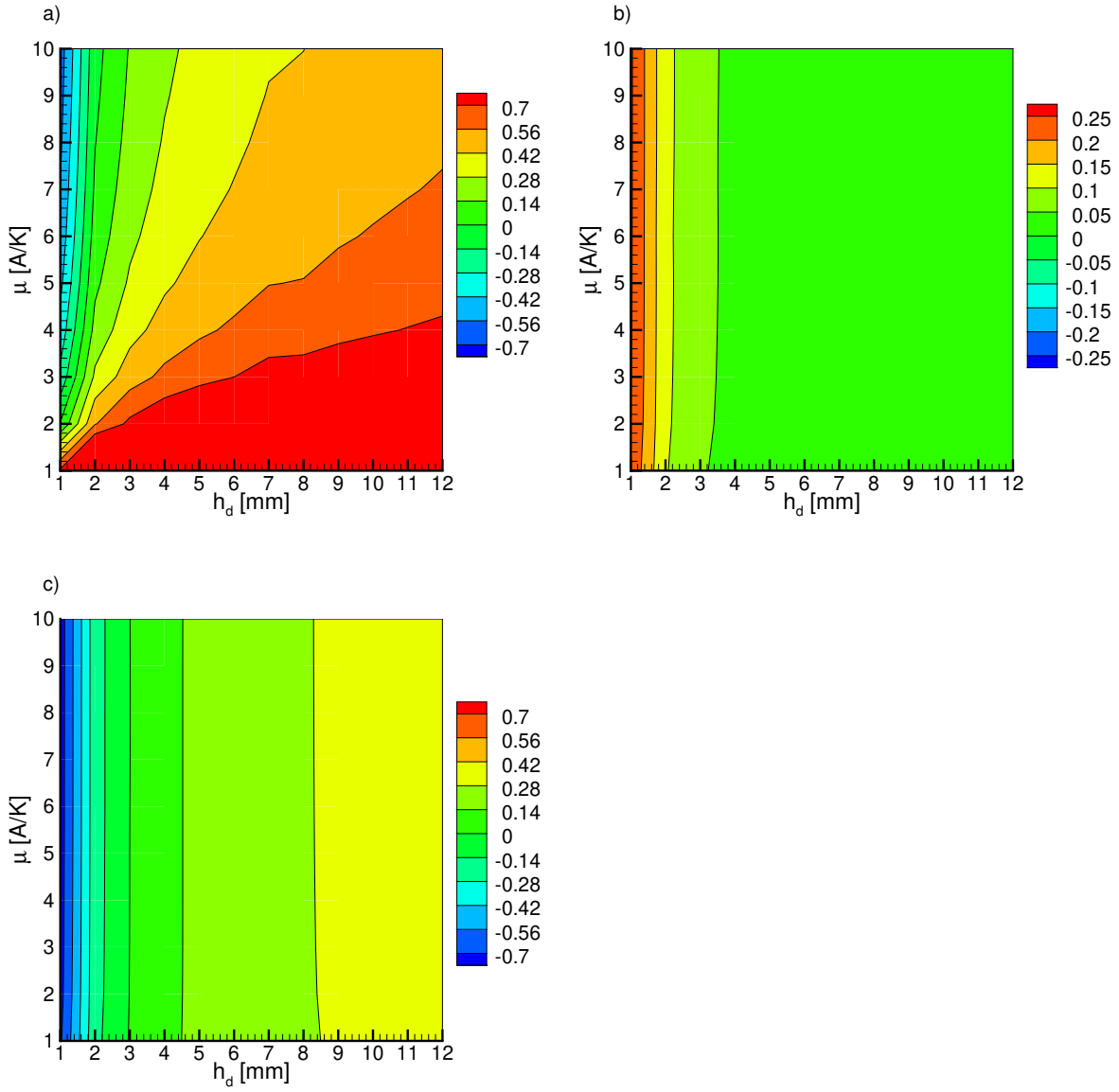

Figure 11: Contour plot of a) ΔT_{ave}, b) $\Delta \bar{T}$ and c) $\Delta T_{ave,m}$ depending on the disc thickness h_d and regulation coefficient μ.

variables, the disc thickness of $h_d = 3mm$ would be the optimal choice for disc diameter of $D_d = 50mm$ and Peltier module Quick-Cool QC-71-1.4-8.5, while the regulation coefficient should be greater than $7A/K$.

4.3 Lesion size

In this section, we tested how the lesion size affects the cooling temperature using an optimal disc thickness of $h_d = 3mm$ for the initial design. Figure 12 shows the average cooling temperature T_{ave} through the cooling process for regulation coefficients $\mu = 4A/K$ and $\mu = 8A/K$ and different lesion sizes, together with healthy skin, where we can observe that the lesion size does not affect the transient cooling temperature. Comparing Clark II and Clark IV melanoma, the temperature difference is almost negligible, and also similar to the cooling temperature of the healthy skin. This is because the lesion does not present a high heat source compared to the cooling heat flow of the Peltier module, for which it does not affect the achieved cooling temperature. Therefore, the achieved cooling temperature on the skin surface using the initial design would be the same for different lesions, and can also be used for different applications of DTI not exceeding the cooling capacity of a Peltier module.

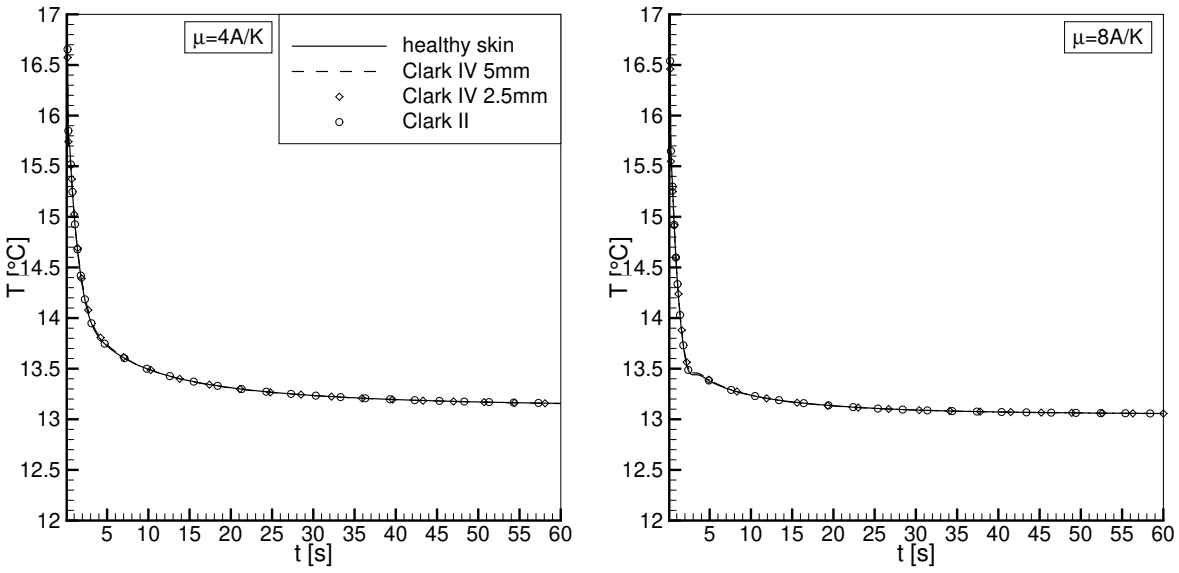

Figure 12: Average cooling temperature T_{ave} through the cooling process for different lesion sizes and healthy skin for different value of μ.

4.4 Cooling depth

For a cooling device of disc thickness $h_d = 3mm$ and regulation coefficient $\mu = 8A/K$ Figure 13 shows a temperature profile through the skin tissue and cooling depth. In Figure 13 a) we can observe a steady-state temperature profile, which is in the range of $35 - 37°C$, as well as the temperature profile during the cooling period at times $10s$, $30s$ and $60s$. It can be seen that the skin (epidermis, papillary and reticular dermis) is cooled down to $13 - 19°C$ during this period. Transient change of cooling depth can be easily observed in Figure 13 b). At

the end of the cooling process ($60s$) the papillary dermis is cooled down to less than $16°C$, while the whole skin to less than $19°C$. Lower temperatures can be achieved by lowering the preset cooling temperature T_{set} or by prolonging the cooling time τ, which affects the temperature contrast during the rewarming period [21]. The papillary dermis is cooled down to less than $17°C$ in $30s$ meaning that for early tumour screening that are located in this layer, the cooling time of $30s$ will be sufficient. However, the cooling time of $\tau = 60s$ using the cooling temperature of $T_{set} = 13°C$ cools down the whole skin and also a portion of fat low enough to produce a good thermal contrast during the rewarming period of DTI for screening early or later tumour stage.

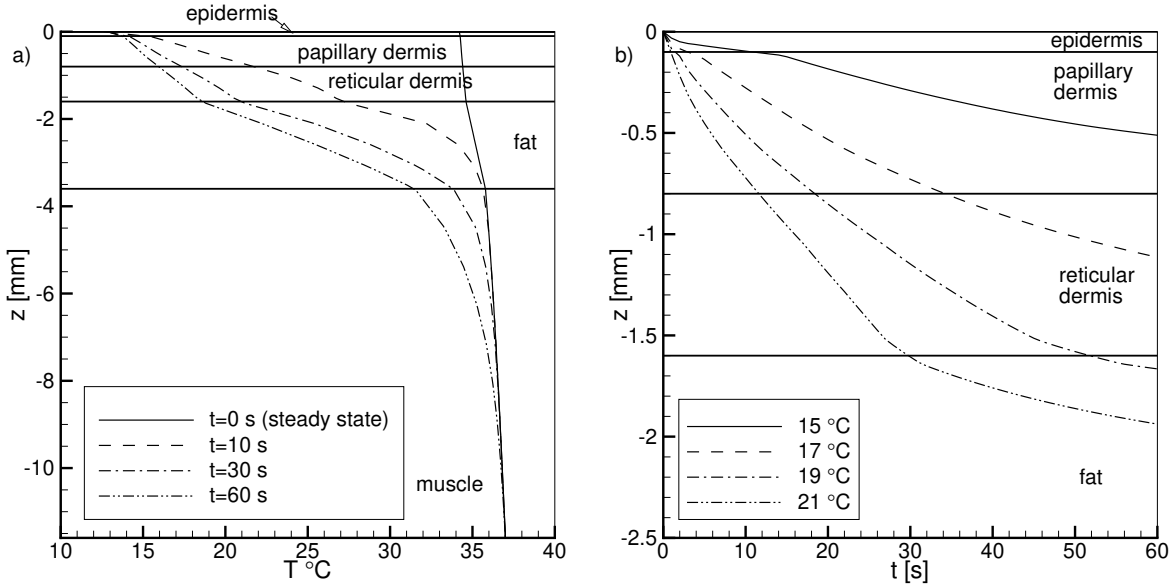

Figure 13: Temperature profile through the skin tissue at different times during the cooling period a) and achieved cooling depth of different isothermal lines through time b) using a device design $h_d = 3mm$ and $\mu = 8A/K$.

5 Conclusion

This paper presents the numerical testing of a cooling device for melanoma screening by DTI. The cooling device cools down the examined tissue to a preset temperature for a certain period of time to increase the temperature contrast of the lesion during the rewarming period, which can easily be observed by an IR camera. Cooling with constant temperature produces deep cooling penetration and therefore good resolution. The focus of this paper is to test the device design composed of metal disc and Peltier module for active cooling, prior to experimental setup or real testing. The goal is to achieve constant and homogenous cooling temperature on the surface during the cooling process of DTI and close to the preset one. The advantage of numerical simulations here is in the prior knowledge of pros and cons of the device design and how to improve it to achieve the desired goal.

The numerical simulation of the proposed cooling device was based on a numerical model composed of skin tissue with melanoma and metal disc as a cooling element, while the Peltier

module was modelled through the boundary conditions. The numerical model has been composed from different layers as well as local thermoregulation of the blood perfusion rate, to model bioheat transfer more realistically. Because of this, a thermal contact resistance between the metal disc and skin tissue has also been imposed to evaluate the cooling design or cooling process as realistically as possible. The numerical model has been solved using a subdomain BEM method, concentrating on the analysis of the design parameters, like position of the thermocouple and how the thickness of the disc or regulation coefficient affect the device response and the achieved cooling temperature on the skin surface.

Evaluation of the cooling device has been done based on the average surface cooling temperature around the melanoma, central temperature reflecting temperature non-homogeneity and temperature difference between achieved cooling temperature and thermocouple measurement. The conclusion is that the position of the thermocouple is not so important as the disc thickness and regulation coefficient to achieve a cooling temperature close to the preset one. From a practical point of view, it can be located on the disc surface near the Peltier module. More important effect in cooling speed and achieved cooling temperature are disc thickness and regulation coefficient. Disc thickness affects the initial cooling due to the thermal capacity and homogeneity of the surface cooling temperature, however, on the other hand, the regulation is slower. Therefore, to achieve a faster response and regulation, a thinner disc is advised.

The analysis showed that thermocouple position P1, disc thickness of $3mm$ and high value of regulation coefficient $\mu > 7A/K$ produced very quickly a stable and nearly constant cooling temperature, close to the preset temperature $13°C$. The choice has been made based on three criteria, achieved average cooling temperature, temperature non-homogeneity and temperature difference between the cooling temperature and disc temperature measurement. The analysis also shows that lesion size in this case does not affect the cooling temperature, which is desirable as it can also be used in other DTI applications not exceeding the cooling capacity of the Peltier element.

Based on the analyses carried out in this paper, future work will be focused on an experimental setup to test the design, to evaluate what is the actual cooling temperature and how it can be evaluated using the temperature measurement of the disc. We show in this paper that cooling temperature is not the same as the temperature measurement of the metal disc, especially at the beginning, however it is very similar in the later stage of the cooling process and can be used to evaluate the actual cooling temperature for experimental tests. As can be seen from this paper, numerical simulation can be very helpful and useful in understanding the phenomena and in improving the cooling technique.

Conflicts of Interest: None
Funding: None
Ethical Approval: Not required

References

[1] W. H. Clark, L. From, E. A. Bernardino, M. C. Mihm, The histogenesis and biologic behavior of primary human malignant melanomas of the skin, Cancer Research 29 (3) (1969) 705–727.

[2] F. Greene, C. Compton, A. Fritz, J. Shah, D. Winchester, Melanoma of the skin, AJCC Cancer Staging Atlas Part V (2006).

[3] M. P. Çetingül, C. Herman, Quantification of the thermal signature of a melanoma lesion, International Journal of Thermal Sciences 50 (4) (2011) 421–431.

[4] C. Fink, H. Haenssle, Non-invasive tools for the diagnosis of cutaneous melanoma, Skin Research and Technology 23 (3) (2017) 261–271.

[5] D. S. Rigel, J. Russak, R. Friedman, The evolution of melanoma diagnosis: 25 years beyond the ABCDs, CA: A Cancer Journal for Clinicians 60 (5) (2010) 301–316.

[6] S. E. Godoy, D. A. Ramirez, S. A. Myers, G. von Winckel, S. Krishna, M. Berwick, R. S. Padilla, P. Sen, S. Krishna, Dynamic infrared imaging for skin cancer screening, Infrared Physics & Technology 70 (2015) 147–152.

[7] A. Breslow, Thickness, cross-sectional areas and depth of invasion in the prognosis of cutaneous melanoma, Annals of Surgery 172 (5) (1970) 902–908.

[8] N. R. Abbasi, H. M. Shaw, D. S. Rigel, R. J. Friedman, W. H. McCarthy, I. Osman, A. W. Kopf, D. Polsky, Early diagnosis of cutaneous melanoma: revisiting the ABCD criteria, Jama 292 (22) (2004) 2771–2776.

[9] C. Herman, The role of dynamic infrared imaging in melanoma diagnosis, Expert Review of Dermatology 8 (2) (2013) 177–184.

[10] J. E. Mayer, S. M. Swetter, T. Fu, A. C. Geller, Screening, early detection, education, and trends for melanoma: current status (2007-2013) and future directions: Part I. Epidemiology, high-risk groups, clinical strategies, and diagnostic technology, Journal of the American Academy of Dermatology 71 (4) (2014) 599.e1–599.e12.

[11] I. Tromme, L. Sacré, F. Hammouch, C. Legrand, L. Marot, P. Vereecken, I. Theate, P. van Eeckhout, P. Richez, J.-F. Baurain, et al., Availability of digital dermoscopy in daily practice dramatically reduces the number of excised melanocytic lesions: results from an observational study, British Journal of Dermatology 167 (4) (2012) 778–786.

[12] A. Kardynal, M. Olszewska, Modern non-invasive diagnostic techniques in the detection of early cutaneous melanoma, Journal of Dermatological Case Reports 8 (1) (2014) 1.

[13] A. Saez, C. Serrano, B. Acha, Model-based classification methods of global patterns in dermoscopic images, IEEE Trans. Med. Imaging 33 (5) (2014) 1137–1147.

[14] E. L. Psaty, A. C. Halpern, Current and emerging technologies in melanoma diagnosis: the state of the art, Clinics in Dermatology 27 (1) (2009) 35–45.

[15] G. Pellacani, B. De Pace, C. Reggiani, A. M. Cesinaro, G. Argenziano, I. Zalaudek, H. P. Soyer, C. Longo, Distinct melanoma types based on reflectance confocal microscopy, Experimental Dermatology 23 (6) (2014) 414–418.

[16] V. Ahlgrimm-Siess, M. Laimer, E. Arzberger, R. Hofmann-Wellenhof, New diagnostics for melanoma detection: from artificial intelligence to RNA microarrays, Future Oncology 8 (7) (2012) 819–827.

[17] M. Carrara, A. Bono, C. Bartoli, A. Colombo, M. Lualdi, D. Moglia, N. Santoro, E. Tolomio, S. Tomatis, G. Tragni, et al., Multispectral imaging and artificial neural network: mimicking the management decision of the clinician facing pigmented skin lesions, Physics in Medicine & Biology 52 (9) (2007) 2599.

[18] R. E. Hunger, R. D. Torre, A. Serov, T. Hunziker, Assessment of melanocytic skin lesions with a high-definition laser doppler imaging system, Skin Research and Technology 18 (2) (2012) 207–211.

[19] B. Lahiri, S. Bagavathiappan, T. Jayakumar, J. Philip, Medical applications of infrared thermography: A review, Infrared Physics & Technology 55 (4) (2012) 221–235.

[20] C. Magalhaes, R. Vardasca, J. Mendes, Recent use of medical infrared thermography in skin neoplasms, Skin Research and Technology 24 (4) (2018) 587–591.

[21] T.-Y. Cheng, C. Herman, Analysis of skin cooling for quantitative dynamic infrared imaging of near-surface lesions, International Journal of Thermal Sciences 86 (2014) 175–188.

[22] J. March, M. Hand, D. Grossman, Practical application of new technologies for melanoma diagnosis: Part I. Noninvasive approaches, Journal of the American Academy of Dermatology 72 (6) (2015) 929–941.

[23] M. Bonmarin, F.-A. Le Gal, Lock-in thermal imaging for the early-stage detection of cutaneous melanoma: A feasibility study, Computers in Biology and Medicine 47 (2014) 36–43.

[24] G. Shi, F. Han, C. Liang, L. Wang, K. Li, A novel method of thermal tomography tumor diagnosis and its clinical practice, Applied Thermal Engineering 73 (1) (2014) 408–415.

[25] J. F. Head, F. Wang, C. A. Lipari, R. L. Elliott, The important role of infrared imaging in breast cancer, IEEE Engineering in Medicine and Biology Magazine 19 (3) (2000) 52–57.

[26] A. Di Carlo, Thermography and the possibilities for its applications in clinical and experimental dermatology, Clinics in Dermatology 13 (4) (1995) 329–336.

[27] J. R. Keyserlingk, P. Ahlgren, E. Yu, N. Belliveau, M. Yassa, Functional infrared imaging of the breast: Historical perspectives, current application and future considerations, CRC Press, 2006.

[28] R. Hatwar, C. Herman, Inverse method for quantitative characterisation of breast tumours from surface temperature data, International Journal of Hyperthermia 33 (7) (2017) 1–17.

[29] A. Amri, S. H. Pulko, A. J. Wilkinson, Potentialities of steady-state and transient thermography in breast tumour depth detection: A numerical study, Computer Methods and Programs in Biomedicine 123 (2016) 68–80.

[30] H. Wang, D. R. Wade Jr, J. Kam, IR imaging of blood circulation of patients with vascular disease, in: Defense and Security, International Society for Optics and Photonics, 2004, pp. 115–123.

[31] M. Bonmarin, F.-A. Le Gal, Thermal Imaging in Dermatology, in: Imaging in Dermatology, Elsevier, 2016, pp. 437–454.

[32] M. Kaczmarek, A. Nowakowski, Active IR-thermal imaging in medicine, Journal of Nondestructive Evaluation 35 (1) (2016) 19.

[33] T. M. Buzug, S. Schumann, L. Pfaffmann, U. Reinhold, J. Ruhlmann, Functional infrared imaging for skin-cancer screening, in: Engineering in Medicine and Biology Society, 2006. EMBS'06. 28th Annual International Conference of the IEEE, IEEE, 2006, pp. 2766–2769.

[34] G. Santa Cruz, J. Bertotti, J. Marin, S. Gonzalez, S. Gossio, D. Alvarez, B. Roth, P. Menéndez, M. Pereira, M. Albero, et al., Dynamic infrared imaging of cutaneous melanoma and normal skin in patients treated with BNCT, Applied Radiation and Isotopes 67 (7) (2009) S54–S58.

[35] K. Ammer, E. Ring, Standard procedures for infrared imaging in medicine, CRC Press, 2006.

[36] M. Strąkowska, R. Strąkowski, M. Strzelecki, G. De Mey, B. Więcek, Evaluation of perfusion and thermal parameters of skin tissue using cold provocation and thermographic measurements, Metrology and Measurement Systems 23 (3) (2016) 373–381.

[37] A. Bhowmik, R. Repaka, Estimation of growth features and thermophysical properties of melanoma within 3-D human skin using genetic algorithm and simulated annealing, International Journal of Heat and Mass Transfer 98 (2016) 81–95.

[38] J. Iljaž, L. C. Wrobel, M. Hriberšek, J. Marn, The use of Design of Experiments for steady-state and transient inverse melanoma detection problems, International Journal of Thermal Sciences 135 (2019) 256–275.

[39] J. Iljaž, L. C. Wrobel, T. Gomboc, M. Hriberšek, J. Marn, Solving inverse bioheat problems of skin tumour identification by dynamic thermography, Inverse Problems 36 (3) (2020) 035002.

[40] H. Schnell, J. Zaspel, Cooling extensive burns: Sprayed coolants can improve initial cooling management: A thermography-based study, Burns 34 (4) (2008) 505–508.

[41] H. Zenzie, G. Altshuler, M. Smirnov, R. Anderson, Evaluation of cooling methods for laser dermatology, Lasers in Surgery and Medicine 26 (2) (2000) 130–144.

[42] M. Strąkowska, R. Strąkowski, M. Strzelecki, G. De Mey, B. Więcek, Thermal modelling and screening method for skin pathologies using active thermography, Biocybernetics and Biomedical Engineering 38 (3) (2018) 602–610.

[43] J. Iljaž, L. C. Wrobel, M. Hriberšek, J. Marn, Numerical modelling of skin tumour tissue with temperature-dependent properties for dynamic thermography, Computers in Biology and Medicine 112 (2019) 103367.

[44] M. Strąkowska, A. Kaszuba, B. Wiecek, M. Strzelecki, G. De Mey, System and software for thermal images screening in medicine–application to psoriasis, Quantitative InfraRed Thermography Journal 12 (2) (2015) 127–136.

[45] M. P. Çetingül, C. Herman, A heat transfer model of skin tissue for detection of lesions: Sensitivity analysis, Physics in Medicine & Biology 55 (2010) 5933–5951.

[46] H. H. Pennes, Analysis of tissue and arterial blood temperatures in the resting human forearm, Journal of Applied Physiology 1 (2) (1948) 93–122.

[47] K. Das, S. C. Mishra, Simultaneous estimation of size, radial and angular locations of a malignant tumor in a 3-D human breast – A numerical study, Journal of Thermal Biology 52 (2015) 147–156.

[48] P. W. Partridge, L. C. Wrobel, An inverse geometry problem for the localisation of skin tumours by thermal analysis, Engineering Analysis with Boundary Elements 31 (10) (2007) 803–811.

[49] A. B. C. Silva, J. Laszczyk, L. C. Wrobel, F. L. Ribeiro, A. J. Nowak, A thermoregulation model for hypothermic treatment of neonates, Medical Engineering & Physics 38 (9) (2016) 988–998.

[50] S. B. Wilson, V. A. Spence, A tissue heat transfer model for relating dynamic skin temperature changes to physiological parameters, Physics in Medicine & Biology 33 (8) (1988) 895–912.

[51] J. Werner, M. Buse, Temperature profiles with respect to inhomogeneity and geometry of the human body, Journal of Applied Physiology 65 (3) (1988) 1110–1118.

[52] J. A. Stolwijk, A mathematical model of physiological temperature regulation in man, NASA contractor report, NASA CR-1855.

[53] J. W. Mitchell, T. L. Galvez, J. Hengle, G. E. Myers, K. L. Siebecker, Thermal response of human legs during cooling, Journal of Applied Physiology 29 (6) (1970) 859–865.

[54] D. Fiala, K. J. Lomas, M. Stohrer, A computer model of human thermoregulation for a wide range of environmental conditions: the passive system, Journal of Applied Physiology 87 (5) (1999) 1957–1972.

[55] D. Fiala, G. Havenith, P. Bröde, B. Kampmann, G. Jendritzky, UTCI-Fiala multi-node model of human heat transfer and temperature regulation, International Journal of Biometeorology 56 (3) (2012) 429–441.

[56] J. E. Laszczyk, A. J. Nowak, Computational modelling of neonate's brain cooling, International Journal of Numerical Methods for Heat & Fluid Flow 26 (2) (2016) 571–590.

[57] S. Kikuchi, K. Saito, M. Takahashi, K. Ito, Temperature elevation in the fetus from electromagnetic exposure during magnetic resonance imaging, Physics in Medicine & Biology 55 (8) (2010) 2411–2426.

[58] P. Bernardi, M. Cavagnaro, S. Pisa, E. Piuzzi, Specific absorption rate and temperature elevation in a subject exposed in the far-field of radio-frequency sources operating in the 10-900-MHz range, IEEE Transactions on Biomedical Engineering 50 (3) (2003) 295–304.

[59] J. R. Davis, et al., Copper and copper alloys, ASM international, 2001.

[60] B. Saggin, M. Tarabini, G. Lanfranchi, A device for the skin–contact thermal resistance measurement, IEEE Transactions on Instrumentation and Measurement 61 (2) (2012) 489–495.

[61] J. Iljaž, L. C. Wrobel, M. Hriberšek, J. Marn, Subdomain BEM formulations for the solution of bio-heat problems in biological tissue with melanoma lesions, Engineering Analysis with Boundary Elements 83 (2017) 25–42.

[62] M. Ramšak, J. Ravnik, M. Zadravec, M. Hriberšek, J. Iljaž, Freeze-drying modeling of vial using BEM, Engineering Analysis with Boundary Elements 77 (2017) 145–156.